AIP Advances

Influence of defects on silicon heterojunction solar cell efficiency: Physical model and comparison with data

Cite as: AIP Advances **11**, 015044 (2021); https://doi.org/10.1063/5.0022983
Submitted: 19 August 2020 . Accepted: 20 December 2020 . Published Online: 27 January 2021

Luca Zumbo, Jean-Francois Lerat, Carmelo Connelli, Claudio Colletti, Cosimo Gerardi, and Salvatore Lombardo

COLLECTIONS

Paper published as part of the special topic on Chemical Physics, Energy, Fluids and Plasmas, Materials Science and Mathematical Physics

openaccess

View Online Export Citation CrossMark

ARTICLES YOU MAY BE INTERESTED IN

Implementation of complete Boolean logic functions in single spin–orbit torque device
AIP Advances **11**, 015045 (2021); https://doi.org/10.1063/5.0030016

Narrowing bandgap and enhanced mechanical and optoelectronic properties of perovskite halides: Effects of metal doping
AIP Advances **11**, 015052 (2021); https://doi.org/10.1063/5.0039308

Prediction of structural, electronic and magnetic properties of full Heusler alloys Ir_2YSi (Y = Sc, Ti, V, Cr, Mn, Fe, Co, and Ni) via first-principles calculation
AIP Advances **11**, 015042 (2021); https://doi.org/10.1063/9.0000101

AIP Publishing

© 2021 Author(s).

Influence of defects on silicon heterojunction solar cell efficiency: Physical model and comparison with data

Cite as: AIP Advances 11, 015044 (2021); doi: 10.1063/5.0022983
Submitted: 19 August 2020 • Accepted: 20 December 2020 •
Published Online: 27 January 2021

View Online Export Citation CrossMark

Luca Zumbo,[1,2,a)] Jean-Francois Lerat,[3] Carmelo Connelli,[4] Claudio Colletti,[4] Cosimo Gerardi,[4] and Salvatore Lombardo[1]

AFFILIATIONS

[1]CNR-IMM, VIII Strada 5 Zona Industriale 95121, Catania, Italy
[2]Dipartimento di Fisica e Astronomia, Università di Catania, Via S. Sofia, 64, 95123 Catania, Italy
[3]Univ. Grenoble Alpes, CEA, LITEN, DTS, LHET, INES, F-38000 Grenoble, France
[4]Enel Green Power, Contrada Blocco Torrazze Zona Industriale, 95121 Catania, Italy

[a)]**Author to whom correspondence should be addressed:** luca.zumbo@gmail.com

ABSTRACT

We have studied the influence of defects on silicon heterojunction solar cell efficiency by a method based on the comparison of electroluminescence (EL) image data with a finite element circuit model of solar cell efficiency. For this purpose, a general curve that relates the solar cell efficiency to a parameter representative of the defect strength, i.e., the loss of V_{OC}, ΔV_{OC}, from EL maps is obtained, and it is shown that the efficiency can be predicted with a good degree of confidence.

© 2021 Author(s). All article content, except where otherwise noted, is licensed under a Creative Commons Attribution (CC BY) license (http://creativecommons.org/licenses/by/4.0/). https://doi.org/10.1063/5.0022983

I. INTRODUCTION

The photovoltaic (PV) technology of silicon/thin hydrogenated amorphous (a-Si:H) silicon heterojunction (HJT) solar cells due to its high performance, low production cost, and simple structure has garnered large interest. HJT solar cells consist of a c-Si n-type wafer covered by thin hydrogenated amorphous silicon (a-Si:H) layers deposited on both sides for good surface passivation and junction formation.[1,2] A quantitative evaluation of solar cells with respect to electro-optical performance is the basis for reliable quality control. In particular, the presence of defect states at the interface leads to recombination, which affects solar cell efficiency.[3,4] In general, for the detection of defects in solar cells, electroluminescence (EL) and photoluminescence (PL) imaging, which are very fast characterization tools, are used, with data acquisition times of a few seconds or fewer per sample.[5–16] Therefore, numerous PL or EL based techniques have been recently developed, with the application of various image processing methods.

In Refs. 5–8, new approaches for PL image treatment are shown. In Ref. 5, a correlation between crystal defects of as-cut wafers and the open circuit voltage of the finished cells in multi-crystalline solar cells is shown. In Ref. 9, a contactless PL method for detection of defects and for prediction of the fill factor and efficiency losses for HJT solar cells is presented. In this method, the acquisition of a unique PL image in open-circuit conditions and a coarse graining image treatment are combined, and a defectivity parameter, which quantifies the impact of defective areas on the average PL signal, is determined, and a correlation between efficiency and the defectivity parameter is shown.

Furthermore, the EL imaging technique has been proposed in recent years to highlight the intrinsic and extrinsic defects that degrade the series resistance and diffusion length in multi-crystalline silicon solar cells (with diffusion lengths much shorter than the solar cell thickness).[10–16] In Ref. 10, a method based on EL imaging to determine maps of the local series resistance of large area solar cells is introduced. The method combines the local electroluminescence emission and its derivative with respect to the applied voltage. In Ref. 11, a method for the determination of the minority carrier diffusion length in silicon wafers and in silicon solar cells by

© Author(s) 2021

measuring the ratio of two luminescence images taken with two different spectral filters is described.

In our work, we show that EL maps of HJT solar cells, transformed into local open circuit voltage (V_{OC}) maps, are univocally correlated with the solar cell efficiency. For this purpose, we first provide a direct physical interpretation of the contrast found in the EL images of HJT solar cells. We propose a model that considers that the minority carrier recombination in the HJT solar cells is influenced by the convolution of two different phenomena: the recombination at the n+ a-Si:H/intrinsic a-Si:H/crystalline Si interface (represented by the surface recombination velocity S_P) and the Si bulk recombination (represented by the carrier lifetime τ). Then, we derive a general functional relationship that correlates the EL signal with the local ΔV_{OC}.

Through a finite element circuit model (FEM), in which the overall solar cell is divided into small elements, we evaluate the I–V characteristics of the overall solar cell starting from maps of defectivity derived from EL images. Then, we show a general curve that relates the overall solar cell efficiency and the ΔV_{OC} maps. Finally, we compare the overall calculation with experimental ΔVoc maps derived from EL maps, and we find good agreement with the proposed model.

II. EVALUATION OF ELECTROLUMINESCENCE IMAGES: THE PHYSICAL MODEL

In Fig. 1, the schematic layout of the solar cells used in this work is shown. The n-type crystalline silicon thickness, d, is 160 μm; instead, the silicon amorphous layers are in the order of a few nanometers. For this reason, in the following physical model, we will neglect the amorphous silicon layers and the thickness of the depletion region.

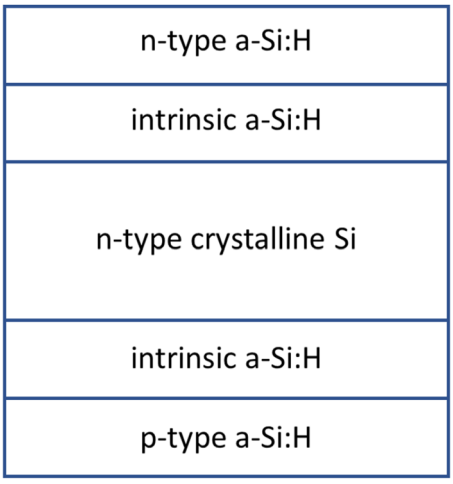

FIG. 1. Schematic diagram of the silicon/thin hydrogenated amorphous (a-Si:H) silicon heterojunction (HJT) solar cells studied in this work. The schematic drawing is not to scale. The n-type crystalline Si is 160 μm thick. The thicknesses of the a-Si:H layers (of the order of a few nm) and of the depletion layers (of the order of a few hundreds of nm) are negligible compared to that of crystalline Si.

As known well,[12] the injection of holes from the p-type a-Si:H/intrinsic a-Si:H/n-type crystalline Si junction (see Fig. 1), $p_n(0)$, at the interface at x = 0 is

$$p_n(0) = \frac{n_i^2}{N_D}\left(\exp\left(\frac{qV}{kT}\right) - 1\right), \tag{1}$$

where n_i is the intrinsic carrier concentration and N_D is the doping concentration, V is the voltage across the junction without considering the ohmic losses, and q is the elementary charge. The rear interface at x = d is characterized by a surface recombination velocity S_P, so at the n + a-Si:H/intrinsic a-Si:H/Si interface, the boundary condition is

$$\frac{dp_n}{dx}\Big|_{x=d} = -\frac{S}{D_p}p_n(d), \tag{2}$$

with D_P being the hole diffusivity. Given these two boundary conditions, from the continuity equation in steady state, the hole distribution $p_n(x)$ is

$$p_n(x) = A\,\sinh\frac{x}{l_p} + B\,\cosh\frac{x}{l_p}, \tag{3}$$

with l being the hole diffusion length and A and B being the integration constants to be determined by the boundary conditions (1) and (2), which are

$$B = \frac{n_i^2}{N_D}\left(\exp\left(\frac{qV}{kT}\right) - 1\right), \tag{4}$$

$$A = \frac{B\left\{1/l_p\,\sinh\left(\frac{d}{l_p}\right) + S_p/D_p\,\cosh\left(\frac{d}{l_p}\right)\right\}}{1/l_p\,\cosh\left(\frac{d}{l_p}\right) + S_p/D_p\,\sinh\left(\frac{d}{l_p}\right)}. \tag{5}$$

In our model, we assume that the measured EL intensity is proportional to the total number of minority carriers in the n-type crystalline Si, that is,

$$\begin{aligned} EL &\propto \frac{\tau_{\exp}}{\tau_{rad}}\int p_n(x)dx \\ &= \frac{\tau_{\exp}}{\tau_{rad}}\left\{Al_p\left[\cosh\left(\frac{d}{l_p}\right) - 1\right] + Bl_p\,\sinh\left(\frac{d}{l_p}\right)\right\}, \end{aligned} \tag{6}$$

where τ_{exp} is the EL image integration time and τ_{rad} is the radiative recombination lifetime.

The dark saturation current density is

$$I_0 = I_{0,p_n} + I_{0,n_p}, \tag{7}$$

where $I_{0,np}$ is the electron diffusion current density in the p-type a-Si:H. Such a term is expected to be many orders of magnitude smaller than the first term, i.e., the hole diffusion current density in the n-type crystalline silicon layer. Therefore, by neglecting such electron current density, we get

$$I_0 \simeq -qD_p\frac{dp_n}{dx}\Big|_{x=0} = q\frac{n_i^2}{N_D}\frac{D_p}{l_p}\frac{S_p\,\cosh\left(\frac{d}{l_p}\right) + D_p/l_p\,\sinh\left(\frac{d}{l_p}\right)}{D_p/l_p\,\cosh\left(\frac{d}{l_p}\right) + S_p\,\sinh\left(\frac{d}{l_p}\right)}. \tag{8}$$

© Author(s) 2021

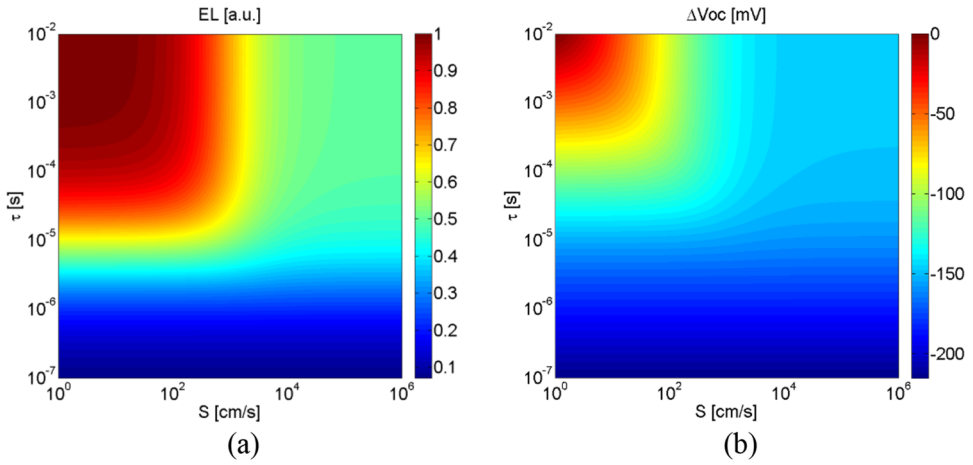

FIG. 2. (a) Electroluminescence intensity as a function of minority carrier lifetime τ and surface recombination velocity S_P. (b) ΔV_{OC} vs τ and S_P.

According to the one diode solar cell model, the open circuit voltage is related to the dark saturation current density, expressed by Eq. (8), and by assuming that the light-generated current density is I_{SC}, we find

$$V_{oc} = \frac{kT}{q} \log\left(\frac{I_{sc}}{I_0}\right). \tag{9}$$

The model of Eqs. (1)–(9) is a one-dimensional model, in which we neglect lateral diffusion of carriers along the y and x directions. Such an assumption is correct if we can neglect the lateral disuniformities in the solar cell. This is surely not exactly true, but since the wafer thickness is low (less than 200 μm), it is realistic to assume that the minority carrier diffusion in the z direction is the dominant effect. It is important to note that the model of Eqs. (1)–(9) shows the nature of the contrast in the electroluminescence image. As shown in Eqs. (6) and (8), the electroluminescence intensity and the dark saturation current density [i.e., the open circuit voltage given by Eq. (9)] depend on two main parameters: the surface recombination velocity S_P and the minority carrier lifetime τ, directly connected to the minority carrier diffusion length l_P, since $l_P = \sqrt{D_P \tau}$.

In Eqs. (1)–(9), several parameters are present. Some of these have values defined in a quite sharp range, so we have decided to fix these to well defined values: $n_i = 1.45 \times 10^{10}\,cm^{-3}$, $N_D = 1 \times 10^{15}\,cm^{-3}$, $\mu_P = 500\,cm^2/Vs$, and $I_{SC} = 40\,mA/cm^2$. On the contrary, τ and S_P can vary in a quite large range, so we have investigated the numerical dependence of EL [Eq. (6)] and ΔV_{OC} [Eqs. (8) and (9)] on these two parameters when these vary by many orders of magnitude. Figures 2(a) and 2(b) show the dependence of EL intensity calculated by Eq. (6) and of ΔV_{OC}, i.e., the difference between each value of V_{OC} and the maximum value of V_{OC} calculated by Eq. (9) on the parameters τ and S_P, both varying in a range of many orders of magnitude. The EL intensity and ΔV_{OC} follow a similar trend: they both increase with lifetime and decrease with the surface recombination velocity. Therefore, given the similarity of the two trends, we can eliminate the τ and S_P variables, and we can plot the EL intensity directly as a function of ΔV_{OC}. Figure 3 reports such a relationship between EL intensity and ΔV_{OC} for the very same data points of Fig. 2. An overall S-shape trend is evident, although the EL = f(ΔV_{OC}) function is not a monotonic function and therefore not strictly invertible. That is, from a purely mathematical point of view, we cannot rigorously find ΔV_{OC} = g(EL). However, as shown in Fig. 2, in the ΔV_{OC} range between −220 mV and −170 mV and between −120 mV and 0, the ΔV_{OC}–EL relationship is indeed almost exactly a single value and monotonic function. For this reason, we have decided to make the approximation of taking an average EL = h(ΔV_{OC}) function, taken as follows: we considered the whole ΔV_{OC}–EL set of values, divided it into small subsets with ΔV_{OC} windows of 1 mV width, and took the average EL value, ⟨EL⟩,

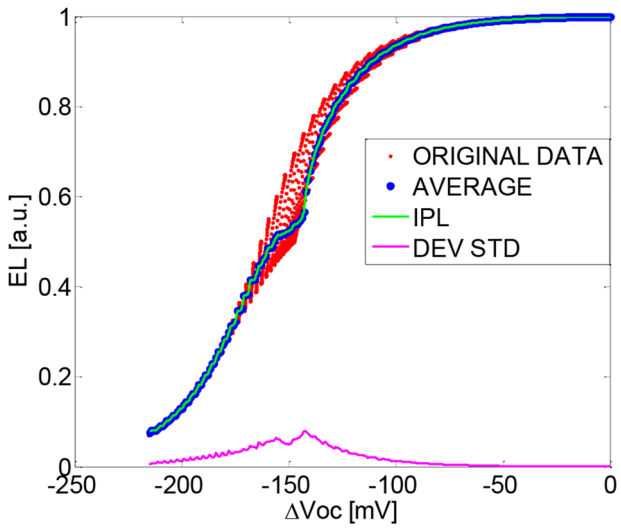

FIG. 3. EL intensity vs ΔV_{OC}. The red data points represent ΔV_{OC} and the EL intensity calculated by the model of Eqs. (6) and (9) and reported in Fig. 2. The blue line is the curve obtained by taking the average EL, ⟨EL⟩, taken in 1 mV ΔV_{OC} intervals (blue data points). The green curve is the linear interpolation curve (IPL) of the ⟨EL⟩–ΔV_{OC} curve.

© Author(s) 2021

for each subset. The resulting ΔV_{OC}–$\langle EL \rangle$ curve is the blue curve reported in Fig. 3, which clearly reproduces quite well the average behavior of the overall ΔV_{OC}–EL set. As further refinement, to calculate ΔV_{OC} corresponding to any particular value of EL, we have considered the linear interpolation curve of the ΔV_{OC}–$\langle EL \rangle$ curve (green curve). In fact, we may also use a specular approach, that is, we can divide the ΔV_{OC}–EL set of values in small subsets of ΔEL windows and take the average $\langle \Delta V_{OC} \rangle$ value for each subset. The resulting $\langle \Delta V_{OC} \rangle$–EL curve is very similar to the ΔV_{OC}–$\langle EL \rangle$ blue curve reported in Fig. 3, although not reported for figure clarity. However, the monotonic behavior is not anymore strictly followed; therefore, we have preferred to use the ΔV_{OC}–$\langle EL \rangle$ curve reported in Fig. 3.

Note that the ΔV_{OC}–$\langle EL \rangle$ relationship represents a calibration method, which transforms the EL signal in a large range of values into a parameter representative of the defect strength, i.e., the loss of V_{OC}, ΔV_{OC}. In the next sections, we discuss the results obtained through this method to study the influence of the defect strength on the HJT solar cell efficiency.

III. PARALLEL DIODE NETWORK MODEL

Here, we present the FEM model to calculate the HJT solar cell efficiency from spatially resolved ΔV_{OC} maps. We consider a $15.6 \times 15.6\,cm^2$ HJT solar cell, and we divide it into a matrix of small solar cells. For each mini-solar-cell, we consider the one diode model. As shown in Fig. 4, the generation current, $I_{pixel(x)}$, of each mini-solar-cell is collected by the metal fingers. The voltage distribution along the fingers, V(x), is obviously ruled by the ohmic loss, which depends on the distance x between the pixel and bus bar. In our approach, we assume that the bus bars are equipotential (no ohmic loss) since generally, this is the contact condition used to collect the EL images on the cells.[3] In particular, we assume that the voltage distribution, V(x) is

$$V(x) = V_{appl} + 2R_M\left[x\int_x^L I_{pixel}(x')dx' + \int_0^x I_{pixel}(x')x'dx'\right], \quad (10)$$

where V_{appl} is the applied voltage, R_M is the metallization line resistance per unit of length, L is the maximum distance from the bus bar, and I_{pixel} is the current for each pixel of a bifacial solar cell, that is,

$$I_{pixel}(x) = I_{SC,pixel}(x) - I_{0,pixel}(x)\left[\exp\left(\frac{qV_{pixel}(x)}{kT}\right) - 1\right], \quad (11)$$

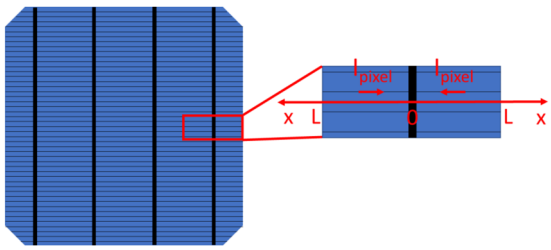

FIG. 4. Schematic diagram of the metallization layout of the HJT solar cell used in this work. The schematic is not to scale.

where $I_{SC,pixel(x)}$ is the light short circuit current, $I_{0,pixel(x)}$ is the dark saturation current, and $V_{pixel}(x)$ is the voltage across the junction for each pixel, that is,

$$V_{pixel}(x) = V(x) + R_S I_{pixel}(x), \quad (12)$$

where R_S is the semiconductor resistance. We have developed a MATLAB tool to solve Eqs. (10)–(12) with an iterative method, which stops at the self-consistency condition. Therefore, through this approach, we are able to calculate from any given arbitrary dark saturation current map, i.e., the ΔV_{OC} map, the resulting overall I–V curve, and the overall efficiency of the HJT solar cell.

IV. RESULTS AND DISCUSSION

N-type silicon wafers ($15.6 \times 15.6\,cm^2$, M2 format) with a thickness of 160 μm were processed on the cell manufacturing pilot-line of CEA and in the Enel Green Power manufacturing line. The HJT cells are in a rear-emitter configuration: the a-Si:H i/p stack was deposited at the rear, and the a-Si:H i/n at the front by PECVD. Indium tin oxide (ITO) is used as TCO, and all cells were metallized on both sides by standard screen-printing of silver paste with a four busbar design.

The EL characterizations were performed on an LIS R2 tool from BT Imaging using an applied voltage of 0.75 V, close to the ideality regime, and with a data acquisition time of 0.5 s.

A. EL image data

Figure 5 shows EL images of HJT solar cells [Figs. 5(a) and 5(b)] and the corresponding ΔV_{OC} maps [Figs. 5(c) and 5(d)] calculated from the EL images by using the ΔV_{OC}–$\langle EL \rangle$ calibration curve of Fig. 3. We performed the analysis both on fresh cells and on the very same cells after scratching them in regions between adjacent fingers to introduce further visible defects in the cells, taking care not to damage the metallization lines, as shown in images of Fig. 5. The defects responsible for recombination appear quite evident in the areas of lower EL intensity and higher local ΔV_{OC}. These are characterized by strengths between 0 mV and 150 mV. Moreover, as expected, the cells after the scratches are characterized by higher local ΔV_{OC} than the fresh cells.

Note that the images need to be corrected in the parts corresponding to the metal bus bars and fingers since these regions obviously correspond to zones of zero EL signal being shadowed by the metal lines.

B. Modeling of EL images

To systematically study the impact of defects on the HJT efficiency, we carried out simulations assuming a random number of defects with random ΔV_{OC} losses and by assuming that I_{SC}, R_M, and R_S are equal for all pixels. The only difference among the pixels is the local V_{OC}.

We have applied a Monte Carlo approach: we have assumed random maps of ΔV_{OC}. In each pixel, ΔV_{OC} is either zero (i.e., V_{OC} is the maximum possible value since there are no defects) or a certain value $\Delta V_{OC\,pixel}$ depending on the probability that a pixel is defective or not. If defective, then, $\Delta V_{OC\,pixel}$ is chosen with the Monte Carlo method, by using a normal distribution of average $\Delta V_{OC\,pixel}$ equal

© Author(s) 2021

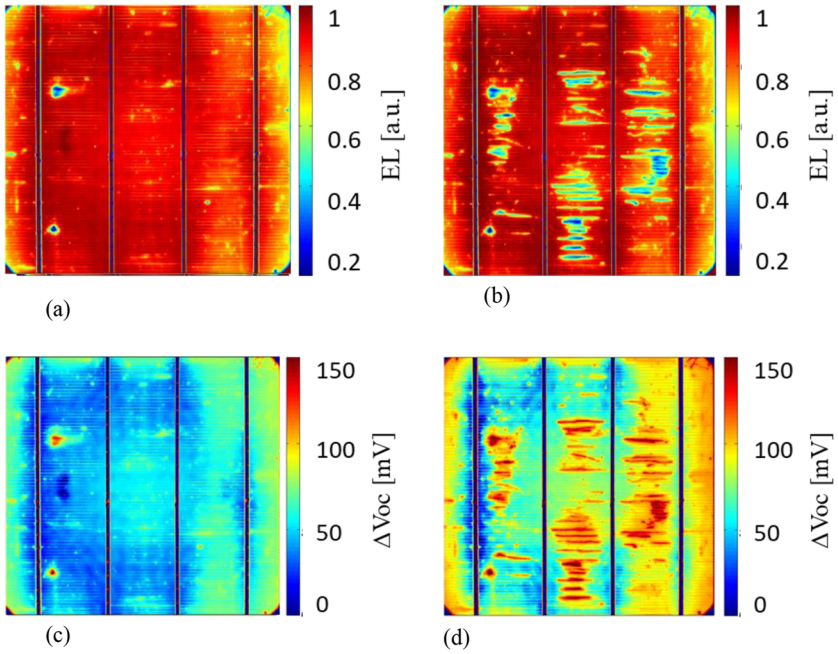

FIG. 5. EL images and ΔVOC maps of the HJT solar cells studied in this experiment. (a) The EL image of the fresh solar cell, without scratches. (b) The EL image of the same solar cell with the scratches. (c) The ΔVOC map of the solar cell without scratches. (d) The ΔVOC map of the same solar cell with the scratches.

to −25 mV, or −50 mV, or −75 mV, or −100 mV and standard deviation equal to 20% of the average. We have also considered the case in which the $\Delta V_{OC\,pixel}$ distribution is uniform in the range 0 mV–100 mV. Once the ΔV_{OC} map is obtained by the Monte Carlo method, then the resulting I–V curve and solar cell efficiency are calculated by using the model described in Sec. III.

To understand the relationship between the overall solar cell efficiency and the ΔV_{OC} maps, we need to find a general functional relationship, which transforms the ΔV_{OC} map into a single number expressing the "defectivity" of the cell. For this purpose, we have identified the following function:

$$\left\langle \Delta V_{oc}^{\gamma} \right\rangle = \frac{\int \Delta Voc_{pixel}^{\gamma} dA}{A}, \tag{13}$$

where γ is a constant and A is the area of the solar cell. In other words, we transform each ΔV_{OC} map into a number, i.e., its average value of ΔV_{OC}^{γ}. To find out the γ value, we have performed a large number of simulations, assuming that the random ΔV_{OC} maps follow Gaussian distributions centered at 25 mV, 50 mV, 75 mV, and 100 mV and with standard deviation equal to 20% of the center or random strength with uniform distribution between 0 mV and 100 mV. As shown in Figs. 6(a)–6(c), all simulations do not follow a unique trend assuming a γ value equal to 1, 1.5, and 2.5. On the contrary, as shown in Fig. 6(d), we find that all simulations follow a unique trend independent of defect average strength when we assume a value for γ equal to about 2. Therefore, based on Fig. 6 results, we conclude that γ is ~2.

We now provide a possible explanation for such a γ value. In fact, since all the pixels are roughly in parallel, in our limit in which we do not consider series resistance changes among the pixels, the overall solar cell power, P, will be the sum of the powers of all microcells,

$$\begin{aligned} P &= \sum_{pixel} I_{pixel} V_{pixel} \\ &= I_{mpp}^{0} V_{mpp}^{0} \sum_{pixel} \left(1 - \frac{\Delta Voc_{pixel}}{\alpha}\right)\left(1 - \frac{\Delta Voc_{pixel}}{\beta}\right), \end{aligned} \tag{14}$$

reduced with respect to the ideal maximum value since there are local losses ΔV_{OC}, which reduce the microcell maximum power point voltage and current, V_{mpp} and I_{mpp}, respectively. Equation (14) is a quadratic functional of ΔV_{OC}; therefore, the γ value that was found, 2, is reasonable when considering Eq. (14).

C. Comparison of EL modeling with experimental data

As discussed above, one expects that for each solar cell fabricated under the same conditions, but generally influenced by random local defects producing carrier recombination generated during the fabrication phase, the experimental average $\langle \Delta V_{OC}{}^2 \rangle$ derived from the EL image and the solar cell efficiency should stay in the trend shown in Fig. 6(c). To verify this point and the overall approach of EL image treatment, we have analyzed a large statistical sample of solar cells fabricated in the same batch with the efficiency equal to 22.5% ± 2% and with the same series resistance R_S within a deviation lower than 6% and with R_S equal to the value used in the FEM simulations. We have also considered some other cells, fabricated in a different batch, but with the same R_S, which were measured in the fresh state and after scratching them in regions between adjacent fingers, to introduce further visible defects in the EL images, taking care not to damage the metallization lines.

Figure 7 shows the overall results. In the graphs, we report the measured solar cell efficiency as a function of average $\langle \Delta V_{OC}{}^2 \rangle$

© Author(s) 2021

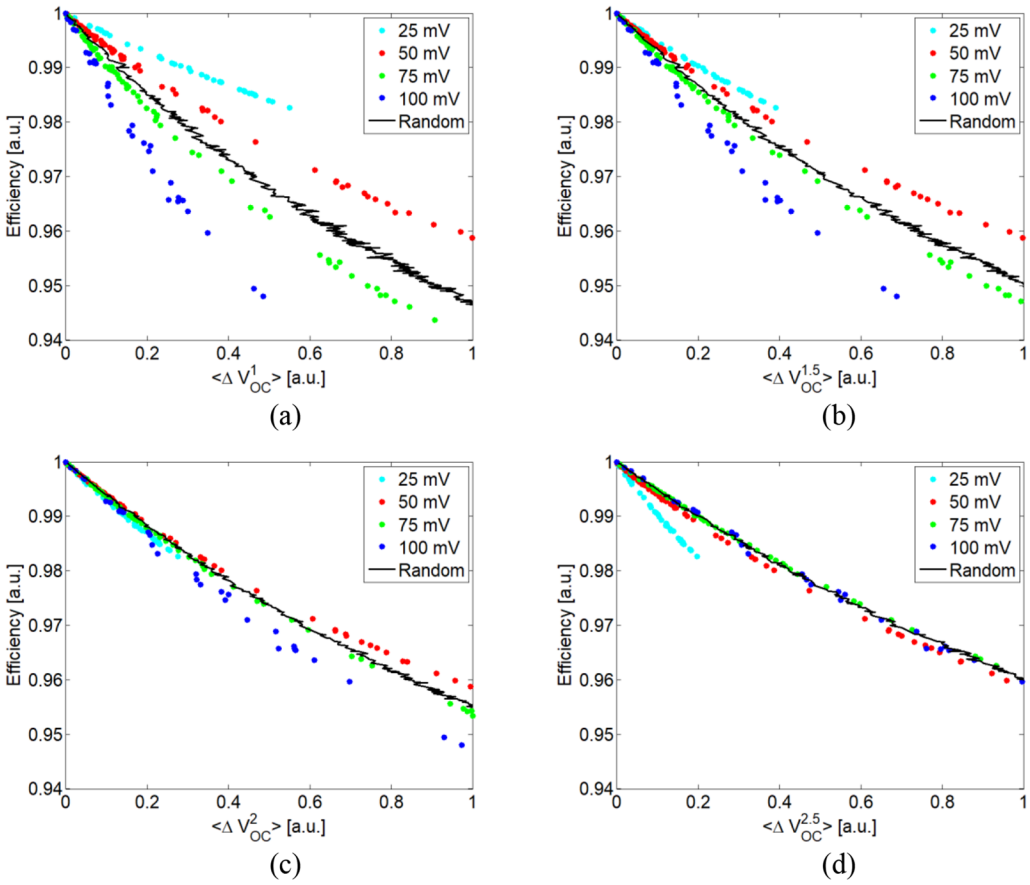

FIG. 6. (a) Simulated efficiency vs $\langle \Delta V_{OC}^{\gamma} \rangle$ calculated by Eq. (13) assuming random rear-surface recombination defects that follow the Gaussian distribution centered at 25 mV, 50 mV, 75 mV, and 100 mV with standard deviation equal to 20% (colored points) of the average and uniform distribution between 0 mV and 100 mV (black line). (a) $\gamma = 1$, (b) $\gamma = 1.5$, (c) $\gamma = 2$, and (d) $\gamma = 2.5$.

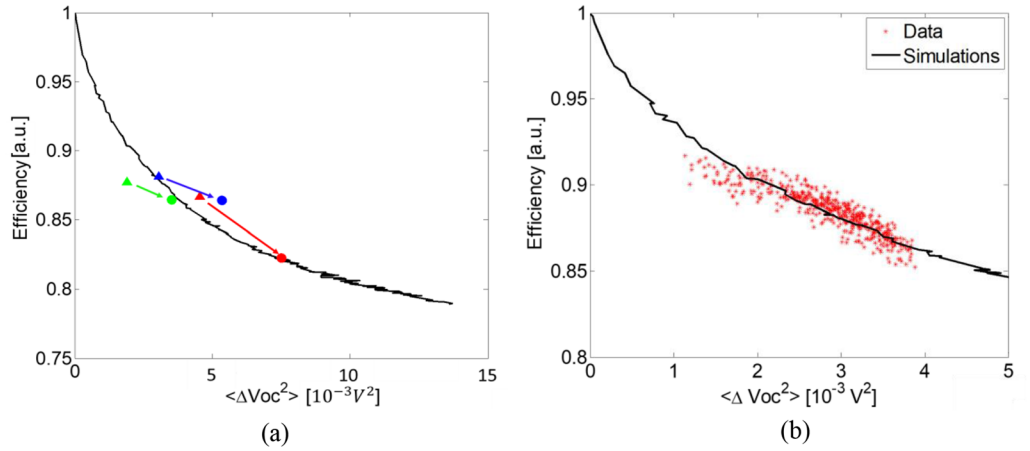

FIG. 7. Comparison between data and simulations. (a) Efficiency vs average $\langle \Delta V_{OC}{}^2 \rangle$ of HJT solar cells with (colored triangular markers) and without (colored circular markers) scratches and simulations (dark line). (b) Efficiency vs average $\langle \Delta V_{OC}{}^2 \rangle$ of a large statistical sample of solar cells fabricated in the same batch and with the same series resistance and simulations (dark line).

© Author(s) 2021

calculated from the EL images and Eq. (13), including both the fresh and the scratched cells, indicated with circles and triangles, respectively, with the same color and with an arrow joining the fresh and scratched cell [Fig. 7(a)]. As shown in Fig. 7(b), we report all the experimental data points (about 1000) of the measured solar cell efficiency as a function of average $\langle \Delta V_{OC}{}^2 \rangle$ calculated from EL images. In the same graphs, we report the theoretical efficiency vs $\langle \Delta V_{OC}{}^2 \rangle$ curve (simulations) calculated according to the proposed model, described in Sec. III, by assuming a uniform random distribution of defects of strength between 0 mV and 200 mV. Good agreement between the data trend and the simulation curve is observed for a γ value of 2. Note that the experimental data of fresh solar cells after scratching move along the model curve, obviously going to lower efficiency values.

V. CONCLUSIONS

We have studied the impact of local defects detected by EL maps on overall solar cell efficiency. We have reported a technique to make a quantitative description of the defect strength and to predict the efficiency through the parallel diode network model. The comparison with experimental data indicates that such a description is effective with a good degree of confidence.

ACKNOWLEDGMENTS

This work was funded by the European Union's Horizon 2020 research and innovation program under Grant Agreement No. 745601 and the project "Automated Photovoltaic Cell and Module Industrial Production to Regain and Secure European Renewable Energy Market" (AMPERE).

The authors declare no conflicts of interest.

DATA AVAILABILITY

The data that support the findings of this study are available from the corresponding author upon reasonable request.

REFERENCES

[1] S. De Wolf, C. Ballif, and M. Kondo, Phys. Rev. B **85**, 113302 (2012).
[2] T. F. Schulze, H. N. Beushausen, C. Leendertz, A. Dobrich, B. Rech, and L. Korte, Appl. Phys. Lett. **96**, 252102 (2010).
[3] J. Haschke, O. Dupré, M. Boccard, and C. Ballif, Solar Energy Mater. Solar Cells **187**, 140–153 (2018).
[4] L. Oppong-Antwi, S. Huang, Q. Li, D. Chi, X. Meng, and L. He, Solar Energy **141**, 222–227 (2017).
[5] J. Haunschildn, M. Glatthaar, M. Demant, J. Nievendick, M. Motzko, and S. Rein, Solar Energy Mater. Solar Cells **94**, 2007 (2010).
[6] M. Turek and D. Lausch, Energy Procedia **38**, 190–198 (2013).
[7] S. Fu, Z. Xiong, Z. Feng, P. J. Verlinden, and Q. Huang, Energy Procedia **38**, 43–48 (2013).
[8] J. Haunschildn, I. E. Reis, T. Chipei, M. Demant, B. Thaidigsmann, M. Linse, and S. Rei, Solar Energy Mater. Solar Cells **106**, 71 (2012).
[9] O. Nos, W. Favre, F. Jay, F. Ozanne, A. Valla, J. Alvarez, D. Muñoz, and P. J. Ribeyron, Solar Energy Mater. Solar Cells **144**, 210–220 (2016).
[10] D. Hinken, K. Ramspeck, K. Bothe, B. Fischer, and R. Brendel, Appl. Phys. Lett. **91**, 182104 (2007).
[11] P. Wurfel, T. Trupke, and T. Puzzer, J. Appl. Phys. **101**, 123110 (2007).
[12] A. Luque and S. Hegedus, *Handbook of Photovoltaic Science and Engineering* (Wiley, 2003).
[13] O. Breitenstein, A. Khanna, Y. Augarten, J. Bauer, J.-M. Wagner, and K. Iwig, Phys. Status Solidi **4**, 7–10 (2010).
[14] M. Glatthaar, J. Haunschild, M. Kasemann, J. Giesecke, W. Warta, and S. Rein, Physica Status Solidi **55**, 85–93 (2010).
[15] M. Glatthaar, J. Giesecke, M. Kasemann, J. Haunschild, W. Warta, and S. Rein, J. Appl. Phys. **105**, 113110 (2009).
[16] M. Glatthaar, J. Haunschild, R. Zeidler, M. Demant, J. Greulich, B. Michl, W. Warta, S. Rein, and R. Preu, J. Appl. Phys. **108**, 014501 (2010).

© Author(s) 2021